

Mitigating Electronic Conduction in Ceria-Based Electrolytes via External Structure Design

Ian A. Robinson, Yi-Lin Huang, Samuel A. Horlick, Jonathan Obenland, Nicholas Robinson, J. Evans Gritton, A. Mohammed Hussain, and Eric D. Wachsman*

Doped ceria electrolytes are the state of the art low-temperature solid oxide electrolytes because of their high ionic conductivity and good material compatibility. However, cerium tends to reduce once exposed to reducing environments, leading to an increase in electronic conduction and a decrease in efficiency. Here, the leakage current is mitigated in ceria-based electrolytes by controlling the defect chemistry through an engineered cathode side microstructure. This functional layer effectively addresses the problematic electronic conduction issue in ceria-based electrolytes without adding significant ohmic resistance and increases the ionic transference $t_{O^{2-}}$ number to over 0.93 in a thin 20 μm ceria-based electrolyte at 500 $^{\circ}\text{C}$, compared to a $t_{O^{2-}}$ of 0.8 for an unmodified one. Based on this design, solid oxide fuel cells (SOFCs) are further demonstrated with the remarkable peak power density of 550 mW at 500 $^{\circ}\text{C}$ and excellent stability for over 2000 h. This approach enables a potential breakthrough in the development of ceria-based low-temperature solid oxide electrolytes.

1. Introduction

Solid oxide electrochemical cells (SOCs) are on the forefront of clean energy research to mitigate the effects of climate change.^[1–6] SOCs can operate in both fuel cell and electrolysis mode (SOFC and SOEC) with high efficiency and provide flexibility in converting energy forms between chemical fuels and electricity.^[1,2,7] Generally, a high temperature is required to thermally activate oxygen ion transportation and electrode reaction processes; however, it also induces degradation issues,^[2,4,8] thus lowering the operating temperatures would significantly advance commercialization of this technology.^[8]

A major challenge of lowering the operating temperature is the significant electrolyte ohmic loss that limits the

performance. Among all solid electrolytes, doped ceria, such as $\text{Ce}_{1-x}\text{Gd}_x\text{O}_{2-\delta}$ (GDC) and $\text{Ce}_{1-x}\text{Sm}_x\text{O}_{2-\delta}$ (SDC), are more attractive options for low-temperature applications than zirconia-based electrolytes, $\text{Zr}_{1-x}\text{Y}_x\text{O}_{2-\delta}$ (YSZ), due to their superior (orders of magnitude higher) oxygen ion conductivity.^[9,10] However, ceria-based electrolytes are mixed ionic and electronic conductors (MIEC) as cerium undergoes $\text{Ce}^{4+}/\text{Ce}^{3+}$ redox couple under reducing conditions.^[11,12] In turn, this causes the open circuit voltage (V_{OC}) of SOCs to be lower than theoretical, decreasing the efficiency of the device.^[13] In addition, for SOECs where electricity is converted into chemical potentials, the electronic conduction in the electrolyte drastically lowers the oxygen ion transference number and makes ceria-based electrolytes impractical to function in electrolysis mode because of lower Faradaic Efficiency.^[12] The theoretical voltage (V_t) is determined by the chemical potential difference between two electrodes and can be expressed by the Nernst equation:

$$V_t = -\frac{RT}{nF} \ln \left(\frac{P_{O_2 \text{ Anode}}}{P_{O_2 \text{ Cathode}}} \right) \quad (1)$$

where R is gas constant, T is temperature, n is the charge of transporting species, F is the Faraday constant, and p_{O_2} represent oxygen partial pressure on either side of the cell.^[5] The cell voltage can be calculated by considering the apparent ionic transference number of the cell electrolyte ($t_{O^{2-}}$) and V_t :

$$V_{OC} = V_t * t_{O^{2-}} \quad (2)$$

I. A. Robinson, Y.-L. Huang, S. A. Horlick, J. Obenland, N. Robinson, J. E. Gritton, A. M. Hussain, E. D. Wachsman
Maryland Energy Innovation Institute
University of Maryland
College Park, MD 20742, USA
E-mail: ewach@umd.edu

I. A. Robinson, Y.-L. Huang, J. E. Gritton, A. M. Hussain, E. D. Wachsman
Department of Materials Science & Engineering
University of Maryland
College Park, MD 20742, USA
S. A. Horlick, E. D. Wachsman
Department of Chemical and Biomolecular & Engineering
University of Maryland
College Park, MD 20742, USA

A. M. Hussain
Advanced Materials and Technology Research
Nissan Technical Centre North America
Farmington Hills, Michigan 48331, USA

The ORCID identification number(s) for the author(s) of this article can be found under <https://doi.org/10.1002/adfm.202308123>

© 2023 The Authors. Advanced Functional Materials published by Wiley-VCH GmbH. This is an open access article under the terms of the Creative Commons Attribution License, which permits use, distribution and reproduction in any medium, provided the original work is properly cited.

DOI: 10.1002/adfm.202308123

Where $t_{\text{O}^{2-}}$ represents the integrated ratio of ionic conductivity to total conductivity across the total electrolyte thickness. In the case of MIECs like doped ceria, because of the different degrees of $\text{Ce}^{4+}/\text{Ce}^{3+}$ redox states under the operational electrochemical potential gradient, the total electronic conductivity of the electrolyte is directly affected by thickness, gas environments on either side, and temperature^[14] and impacts efficiency unless the electronic leakage current is mitigated.^[15–18] For example, an SOFC at 650 °C with a 10 μm thick GDC electrolyte has a V_{OC} of only 0.79 V and simply doubling the GDC thickness for an identical SOFC to 20 μm increases the V_{OC} to 0.86 V.^[17] This increase in V_{OC} is due to a higher apparent $t_{\text{O}^{2-}}$ as cerium reduction is limited to the near anode region with a thicker region of higher localized $t_{\text{O}^{2-}}$ toward the cathode side as total thickness increases, however, it also contributes to a higher ohmic loss which severely penalizes the performance at low temperatures.^[15–17]

One approach is to find new materials that have a high $t_{\text{O}^{2-}}$, but so far there is no single candidate that meets all criteria for low-temperature solid electrolytes. Another approach is to reduce the thickness of conventional YSZ electrolytes. To limit the ohmic loss ($<0.1 \Omega \text{ cm}^2$ at 500 °C), the dense, defect-free, YSZ thin film needs to be $<1 \mu\text{m}$,^[19] which is very challenging using traditional, scalable ceramic processing techniques. The other approach is to modify the defect chemistry of the known electrolytes, such as introducing different dopants in ceria. For instance, $\text{Pr}_x\text{Ce}_{1-x}\text{O}_{2-\delta}$ (PCO), $x < 0.01$ has been reported to have a high $t_{\text{O}^{2-}} \approx 1$ in the high $p\text{O}_2$ regime. However, PCO displays a lower ionic conductivity than GDC (approximately $2/3 \sigma_{\text{ion}}$), and in the low $p\text{O}_2$ regime the $t_{\text{O}^{2-}}$ is significantly less than that of GDC (~ 0.4 at 10^{-15} atm), making PCO an unsuitable electrolyte for low temperature SOFCs.^[20] Despite various attempts to increase the intrinsic $t_{\text{O}^{2-}}$ of doped ceria, they have not prevented the Ce^{4+} reduction, and the resulting leakage current has been the necessary sacrifice for using high-oxygen conducting ceria-based electrolytes.

Here we address the leakage current issue in ceria-based electrolytes and demonstrate that the electronic conduction of ceria-based electrolytes can be mitigated via design of an external cathodic side structure, reaching a $t_{\text{O}^{2-}} = 0.93$ for a 20 μm GDC at 500 °C. We engineer a porous function layer (PFL) on the cathode side that increases exposure of this ceria layer to higher effective $p\text{O}_2$ and show that the intrinsic electron charge carrier density in this porous layer is significantly lower because of the gas-solid equilibrium of the PFL in air. In addition, by engineering the PFL with active dopants (Pr), the Pr in the PFL facilitate oxygen transport and shows synergistic effects to significantly enhance the cell performance. These two results lead to a system exhibiting a much higher V_{OC} , lower area specific resistance (ASR), higher performance, and increased durability, achieving $>2000 \text{ h}$ of cell operation with no performance losses.

2. Results and Discussion

For materials like doped ceria, dominant defects are controlled by the oxygen stoichiometry, x , in $\text{Ce}(\text{Gd})\text{O}_{2-x}$. These defects are the main charge carriers that determine the electronic and ionic conductivity. In reducing conditions, the reduction of Ce^{4+} to Ce^{3+} significantly increases the electronic conductivity. From the

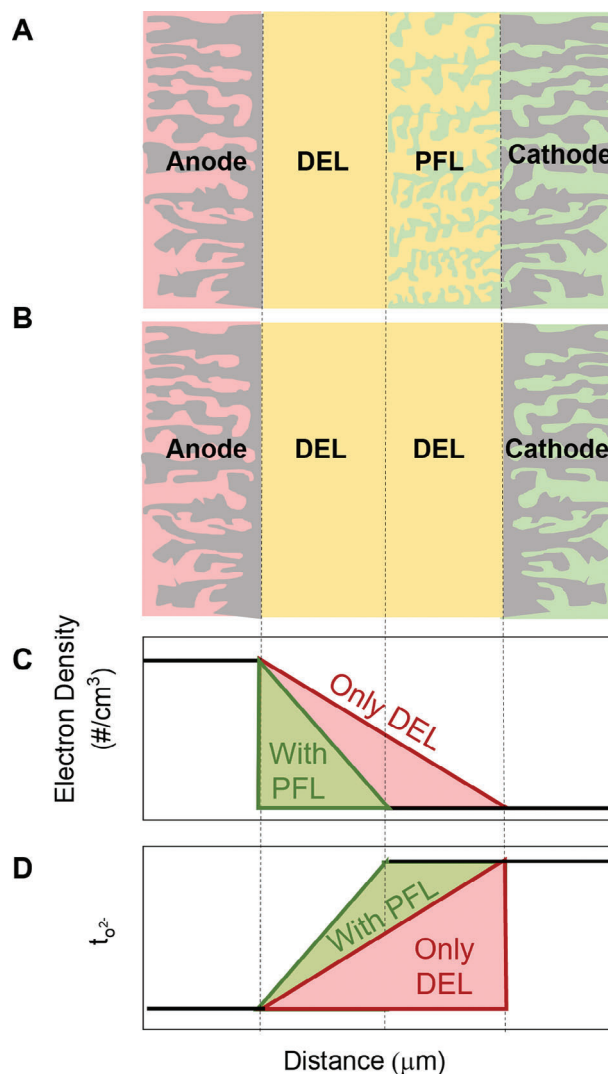


Figure 1. Electronic Conduction Mitigation via External Structure Design. Schematic drawing of the cell configuration A) with PFL and B) without PFL. C) The corresponding change in electron charge carrier density and D) transference number as a result of porous structure based on the simplified defect model. Note the profiles are simplified to linear to clearly show the concept.

solid-state chemistry point of view, as $p\text{O}_2$ decreases, the electron charge carrier concentration, n , increases with x to accommodate the formation of positively charged oxygen vacancies. In contrast, in the high $p\text{O}_2$ regime, the high oxygen chemical potential maintains a low level of x , and thus limits the electronic conductivity of doped ceria.

Figure 1A,B shows conceptual schematics of cases with and without a PFL. The operating gas environments for the SOFC cathode and anode are highlighted in light green and red, respectively. In the case of PFL, Figure 1A, oxygen molecules can freely diffuse through the pores, and a homogeneous $p\text{O}_2$ and thus stoichiometry of this porous layer is achieved. Therefore, the entire PFL has a constant defect concentration as it is exposed to the same environment, i.e., $p\text{O}_2 = 0.21 \text{ atm}$. In contrast, for the case

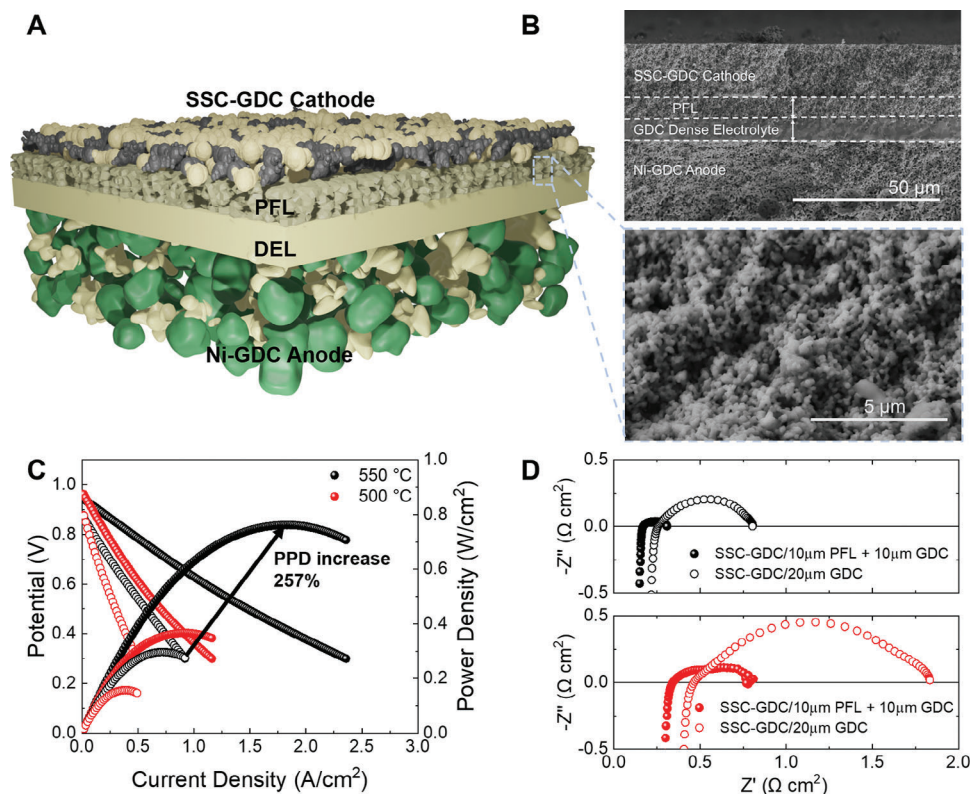


Figure 2. SOFC Design, Microstructure, and Electrochemical Performance. A) SOFC design with the PFL. B) Cross-section SEM image of the cell microstructure: 20 μm SSC-GDC cathode, 10 μm Pr-GDC PFL, 10 μm GDC electrolyte, 20 μm anode functional layer (AFL), and 500 μm Ni-GDC anode. The enlarged view of the PFL microstructure is also shown. C) Current–voltage (I–V) behavior at 500, 550 $^{\circ}\text{C}$ (red and black, respectively) shown for the 20 μm GDC in open symbols and 10 μm DEL + 10 μm PFL (with 0.5 wt.% PrO_{2-x}). D) EIS spectra at both 500 and 550 $^{\circ}\text{C}$ (red and black, respectively), shown for the 20 μm DEL and 10 μm DEL + 10 μm PFL (open and closed symbols, respectively).

with only a dense electrolyte layer (DEL) in Figure 1B, the air environment only extends to the cathode/electrolyte interface.

The advantage of the PFL can be clearly seen in the plots of electron charge carrier density and $t_{\text{O}^{2-}}$ versus distance in Figure 1C,D, respectively, which are shown for simplicity as linear. The areas underneath the curves represent the relative electron charge carrier concentration and average transference numbers in the electrolytes. With the PFL, the oxygen chemical potential boundary condition of the cathode gas environment is now extended from the cathode/electrolyte interface to the DEL/PFL interface because of the porous nature of the PFL. This change provides an extended electrolytic region significantly lower in electron charge carrier density, as shown by the green lines. As a result, the effective $t_{\text{O}^{2-}}$ increases, and this enhancement in ionic/electronic conductivity ratio significantly improves the efficiency of ceria-based electrolytes.

In addition, as the PFL extends the cathodic $p\text{O}_2$ throughout its structure providing opportunity to utilize the higher $t_{\text{O}^{2-}}$ of Pr doped ceria in this structure without the negative effect on ionic conductivity of having Pr on low $p\text{O}_2$ side of a dense electrolyte.^[20] This is also explored here.

To examine this concept, we used a typical SOFC and conventional low-temperature electrode materials with a configuration of $\text{Sr}_{0.5}\text{Sm}_{0.5}\text{CoO}_{3-\delta}-\text{Ce}_{0.9}\text{Gd}_{0.1}\text{O}_{2-\delta}$ (SSC-GDC)/GDC/Ni-GDC and inserted a PFL, as shown in the cell architecture in

Figure 2A. The scanning electron microscopy (SEM) image in Figure 2B, highlights the discrete layers of cathode, PFL, DEL and anode. The microstructure of the PFL is also shown, detailing the porous nature of the layer. Two cells are tested with the same total GDC thickness: one configured with 10 μm DEL + 10 μm PFL (Figure 1A), and the other configured with a 20 μm DEL (Figure 1B). Results shown in Figure 2C highlight the impact of the porous engineered microstructure.

The PFL provides two performance enhancements to the cell, an increase in V_{OC} and a decrease in impedance. The V_{OC} increases from 0.91 to 0.98 V at 500 $^{\circ}\text{C}$ and from 0.88 to 0.95 V at 550 $^{\circ}\text{C}$, an 8% improvement because of defect engineering. In addition, by replacing 10 μm of the DEL with PFL, the ohmic ASR drops from 0.25 to 0.17 $\Omega\text{ cm}^2$ at 550 $^{\circ}\text{C}$ and from 0.46 to 0.34 $\Omega\text{ cm}^2$ at 500 $^{\circ}\text{C}$, as shown by electrochemical impedance spectroscopy (EIS) in Figure 2D. Given in both cases the total GDC thickness is the same (20 μm) but in PFL case half that thickness is porous which one would assume would increase ohmic ASR due to constriction of ion transport in porous structure, we assume that with the Pr doping a fraction of the outer PFL contributes to the cathodic ORR reducing the effective electrolyte thickness. This could also be why the non-ohmic polarization with the PFL (0.14 $\Omega\text{ cm}^2$ at 550 $^{\circ}\text{C}$ and 0.47 $\Omega\text{ cm}^2$ at 500 $^{\circ}\text{C}$) is dramatically less than the DEL alone (0.55 $\Omega\text{ cm}^2$ at 550 $^{\circ}\text{C}$ and 1.37 $\Omega\text{ cm}^2$ at 500 $^{\circ}\text{C}$). As a result, addition of the PFL leads

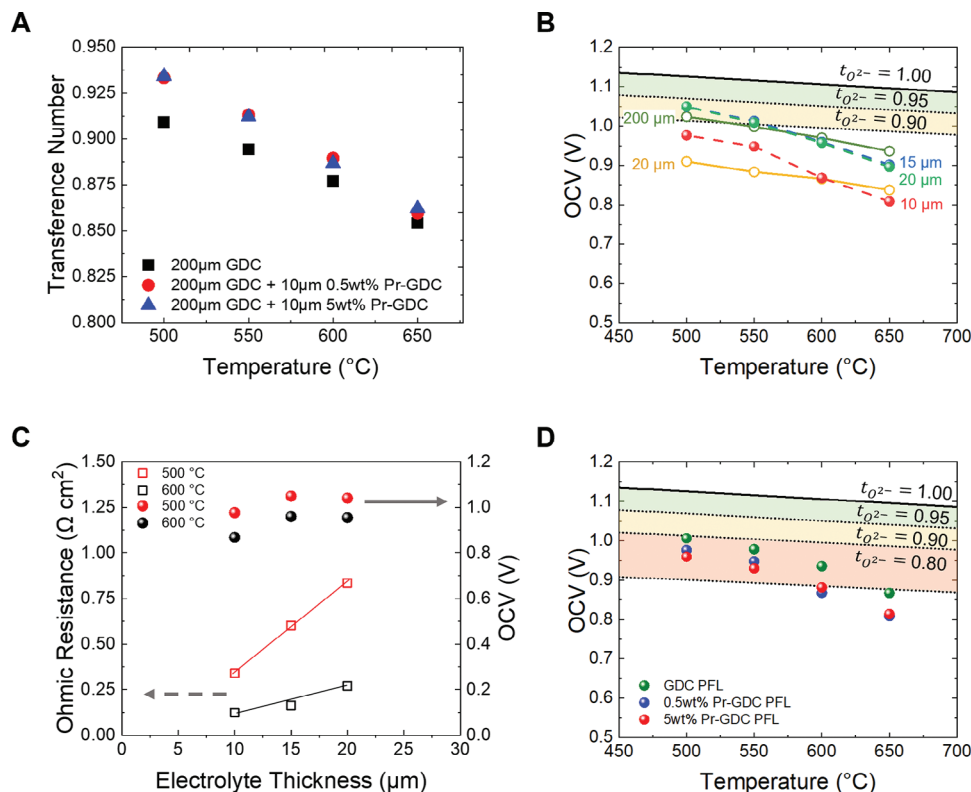


Figure 3. The V_{OC} enhancement via the PFL. A) Transference Number measurement on 10 μm PFL/200 μm GDC. B) V_{OC} Enhancement with PFL on 20 μm GDC with different PFL thicknesses. C) Ohmic loss and V_{OC} enhancement at 500 $^{\circ}\text{C}$ (red) and 600 $^{\circ}\text{C}$ (black) with varying GDC electrolyte thickness paired with 10 μm PFL (with 0.5 wt%PrO_{2-x}). D) V_{OC} versus Temperature for different Pr doping levels in 10 μm PFL with 10 μm DEL.

to a large (as much as 257% at 550 $^{\circ}\text{C}$) increase in peak power density (PPD) – up to 0.36 and 0.76 W cm^{-2} at 500 and 550 $^{\circ}\text{C}$, respectively.

SOFCS with different DEL thicknesses and PFL concentrations (0, 0.5, and 5.0 wt.% Pr) were tested to understand the V_{OC} enhancement mechanism of the PFL (Figure 3). The standard PFL concentration referenced throughout the figures is a (0.5 wt.% Pr₆O₁₁ + GDC) PFL, and all other weight percent configurations are denoted (X wt.% of Pr + GDC). First, we demonstrated the effectiveness of the PFL on V_{OC} enhancement by depositing a 10 μm PFL with different Pr concentrations on a 200 μm GDC support, as shown in Figure 3A. Therefore, by using the PFL the reduction in V_{OC} at low GDC thickness can be minimized.^[17] Due to the MIEC in GDC, apparent ionic transference number, t_{O_2} , of GDC (black dots) reaches only 0.91 V at 500 $^{\circ}\text{C}$. As temperature increases, oxygen non-stoichiometry, x , and electron defects are both thermally activated, leading to the further decrease in t_{O_2} to 0.85 V at 650 $^{\circ}\text{C}$. With the PFL, t_{O_2} improves significantly, and this enhancement is more effective at low temperature even though the PFL is only 5% of the total electrolyte thickness.

Figure 3B shows the PFL effect on V_{OC} for thin anode-supported 20 μm GDC electrolytes with PFL thicknesses from 10 to 20 μm . The GDC baselines of 200 and 20 μm DEL thicknesses are shown by open symbols with solid lines. The theoretical voltage as well as the levels of t_{O_2} are also shown. When the thickness of GDC decreases from 200 to 20 μm , the V_{OC} drops over 10%, due to the higher electrochemical gradient (air/H₂@3%H₂O)

across the thin electrolyte: 5.8 versus 58 $\text{mV } \mu\text{m}^{-1}$ for 200 to 20 μm thick GDC, respectively that forces reduction of Ce⁴⁺/Ce³⁺ redox couple and increases electronic conductivity.

Compared to the 20 μm GDC baseline, the presence of PFL increases V_{OC} at all temperatures. With an increase in DEL thickness to 200 μm the V_{OC} can reach 93% and 90% of theoretical value at 500 and 550 $^{\circ}\text{C}$, respectively. The 15 and 20 μm PFL increases the V_{OC} for a 20 μm thick GDC DEL electrolyte to match that of a 200 μm thick GDC DEL and in fact exceeds it as temperature drops below 600 $^{\circ}\text{C}$. This external structure design enhances the V_{OC} more effectively than simply increasing GDC thickness as the V_{OC} of the 20 μm thick DEL + 15 μm thick PFL (total 35 μm thickness) is higher than that of the 200 μm thick GDC with a significantly lower ASR.

Since the extrinsic structure design can minimize the electron conduction in GDC, we can minimize the thickness of the DEL to minimize ohmic loss for oxygen transport without sacrificing V_{OC} . Figure 3C shows the thickness effect of a 10 μm PFL (0.5wt%PrO_{2-x}-GDC) paired with varying DEL thicknesses. The ohmic ASR depends linearly on varying electrolyte thickness, with the lowest value for the 10 μm DEL sample. Incredibly, the V_{OC} can surpass 1 V with an ohmic ASR of only $\approx 0.3 \Omega \text{ cm}^2$ at 500 $^{\circ}\text{C}$. The V_{OC} of the 15 μm DEL + 10 μm PFL maintains a high V_{OC} , comparable to the V_{OC} of the 20 μm DEL + 10 μm PFL configuration, but without the ohmic losses of a 20 μm thick electrolyte; suggesting that over 15 μm , the DEL has minimum effect on the V_{OC} increase but contributes to ohmic loss.

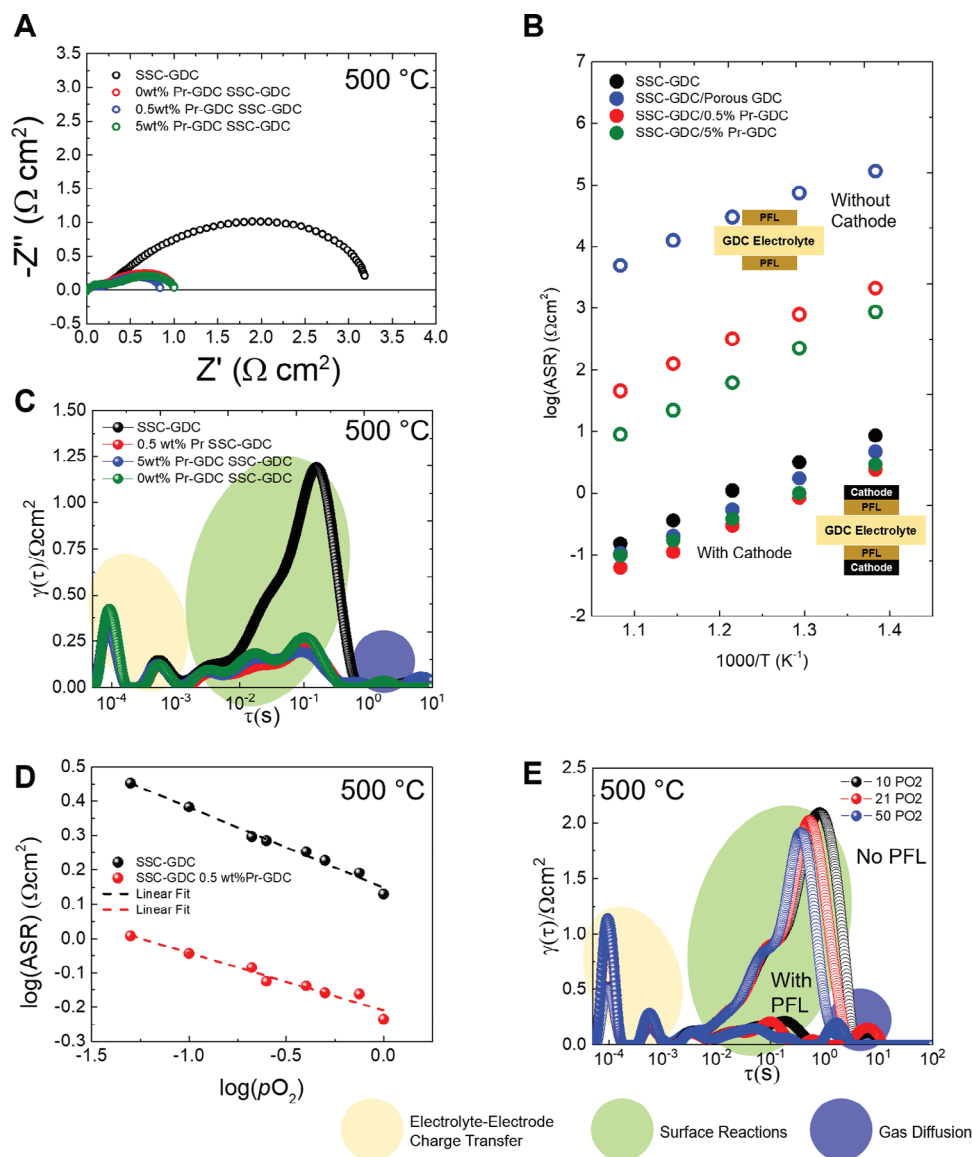


Figure 4. Electrochemical enhancement due to PFL layer composition. A) Nyquist plots at 500 °C of SSC-GDC cathode symmetrical cell with varying Pr doping level in the PFL. B) Arrhenius behavior of SSC-GDC symmetrical cells with or without the PFL. The colors correspond to the concentration of Pr in the Pr-GDC layer and the open symbols account for a situation where the PFL is tested on its own and closed symbols show SSC-GDC on top of the PFL. C) Corresponding DRT analysis in (A). D) pO_2 dependent behavior comparing SSC-GDC with or without PFL at 500 °C and E) corresponding DRT curves.

Figure 3D shows the doping level effect of Pr in the PFL on the V_{OC} enhancement on a 10 μm DEL + 10 μm PFL. Adding Pr as a homogenous dopant in the PFL decreases somewhat the OCV enhancement, suggesting that the external porous structure is the key factor for the decrease in electronic conduction in GDC layers, and the chemical composition of the PFL is not the main cause. Nevertheless, the addition of Pr has a significant benefit on electrochemical performance and will be discussed in the next section.

The PFL effect on the electrochemical performance enhancement was determined using a symmetrical cell configuration. Figure 4A shows Nyquist plot of SSC-GDC cathode with or without the presence of the PFL. The addition of a PFL reduces polar-

ization impedance and Pr concentration in the PFL plays a role in the overall cathode performance. A pure porous GDC layer reduces cathode ASR, likely due to the increase in active area at the cathode triple phase boundary, and the addition of multivalent Pr further enhances the electrochemical performance. The PFL with 0.5 wt.% PrO_{2-x} has the lowest cathode ASR, $0.7 \Omega cm^2$ compared to $3.2 \Omega cm^2$ without a PFL. However, the higher doping level of Pr (5 wt.%) may act as a sintering aide as the microstructure shown in Figure S6D (Supporting Information) appears to densify composition, leading to the decrease in active surface area.

We further tested PFL/GDC symmetrical cells (without SSC-GDC cathode) to separately determine electrochemical activity of

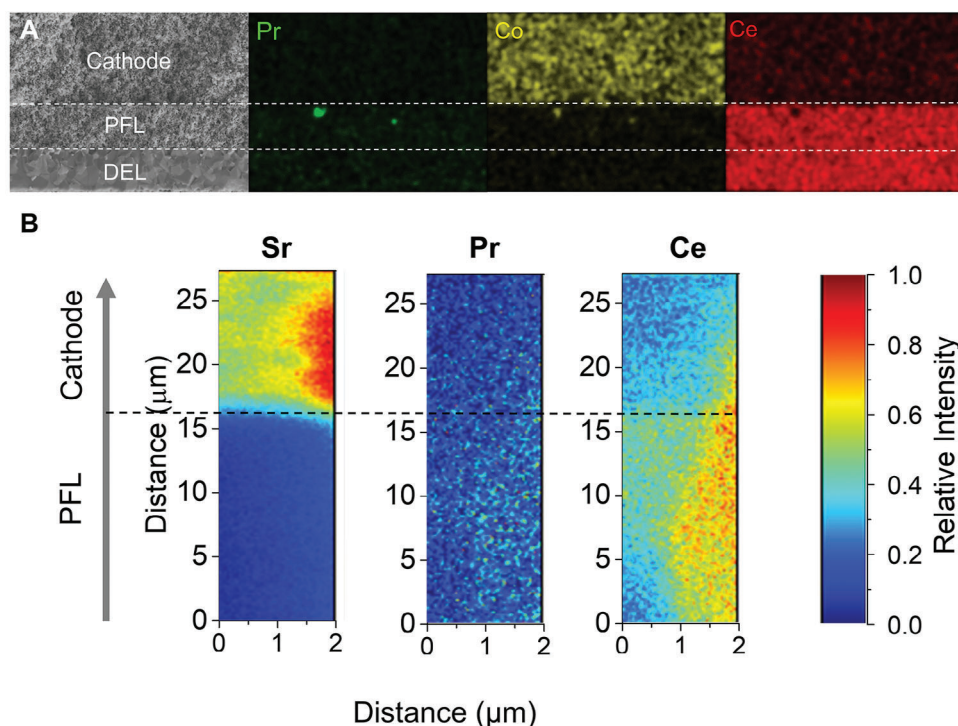


Figure 5. Chemical Analysis of the PFL. A) SEM-EDS of the cathode, PFL, and electrolyte interface with constituent elements from each the cathode, electrolyte, and PFL. B) ToF-SIMS of elemental mapping across the cathode/PFL interface. X-axis and Y-axis represent the planar and the depth profile. The colormap (arbitrary unit) represents the intensity of each element.

the PFL. Arrhenius plot of cathode ASR in Figure 4B displays that the PFL lacks sufficient cathode activity on their own regardless of the Pr doping level as the electrode polarization is 2–3 orders of magnitude higher than the cathode on top of PFL configuration. The impact of Pr is further shown in the same plot, as PFL acting without cathode has an ASR with orders of magnitude higher than conventional SSC-GDC cathode (black dots), highlighting that the PFL does not have sufficient cathode activity on its own. There is further evidence that the PFL does not have sufficient electrochemical activity to function as a cathode and is shown in Figure S3 (Supporting Information). Pr plays a role in increasing cathodic activity in the PFL, evident in Figure S3 (Supporting Information), the electrode ASR decreases from on the order of $\approx 104 \Omega \text{ cm}^2$ at 500 °C in the case of no Pr in the PFL to on the order of $102 \Omega \text{ cm}^2$ at 500 °C for both cases of Pr in the PFL and without SSC-GDC cathode. This suggests that Pr enhances electrochemical activity in the PFL.

The distribution of relaxation times (DRT) analysis in Figure 4C further elucidates how the PFL enhances cathode performance.^[21–26] The SSC-GDC without a PFL (black curve) has the highest overall reaction losses in the region (time constant (τ) = 10^{-3} – 10^0 (s)), which is typically attributed to the surface reaction.^[21,26–28] With the addition of the PFL, this peak intensity decreases, suggesting the PFL facilitates surface reaction steps, which is consistent with previous findings.^[27] Further aging results at 500 and 600 °C are shown in Figure S7 (Supporting Information) for the symmetrical cells aged in this study. It can be seen that the SSC-GDC with PFL is stable on its own for over 1200 h at 500 and 600 °C maintaining electrode ASR's of

≈ 0.8 and $0.25 \Omega \text{ cm}^2$ respectively. The aging result at 600 °C shows that the stability of the SSC-GDC + PFL is significantly enhanced compared to the baseline SSC-GDC.

Isothermal oxygen partial pressure ($p\text{O}_2$) dependent studies and the corresponding DRT analyses are shown in Figure 4D,E to help determine the exact role of the PFL on the cathode performance. Double log plot of cathode ASR versus $\log(p\text{O}_2)$ shows that by adding the PFL, the impedance is lowered at all $p\text{O}_2$'s with a slope change from 1/4 to 1/6, indicating that the change of the rate-limiting-step on the surface reactions.^[29,30] The DRT results deconvolute the impedance results to show that the PFL decreases the reaction losses in the surface reaction region ($\tau = 10^{-3}$ – 10^0 (s)). The ASR dependence and DRT on the $p\text{O}_2$ for both the PFL and standard case are further explored in the Figure S1 (Supporting Information).

Chemical composition analysis is shown in Figure 5 to determine how the microstructure and elemental mapping may indicate improvements in ASR. Figure 5A shows the electron dispersive spectroscopy (EDS) mapping of the elements in each solid oxide layer. A sharp interface between cathode and PFL can be clearly seen based on Co signal. Both PFL and DEL are ceria-based, and the concentration of Pr is too low to be detected using EDS. Further content of Pr in the Pr-GDC layer can be seen in Figure 5B where time of flight secondary ion mass spectroscopy (ToF-SIMS) was performed. Y-axis represents the depth and the colormap is the signal intensity of each element. Sr, Pr, and Ce are shown in this mapping where the Sr signal discretely exists only in the cathode. The sharp cathode/PFL interface indicates there is no interdiffusion of Sr. Ce appears in both the PFL and

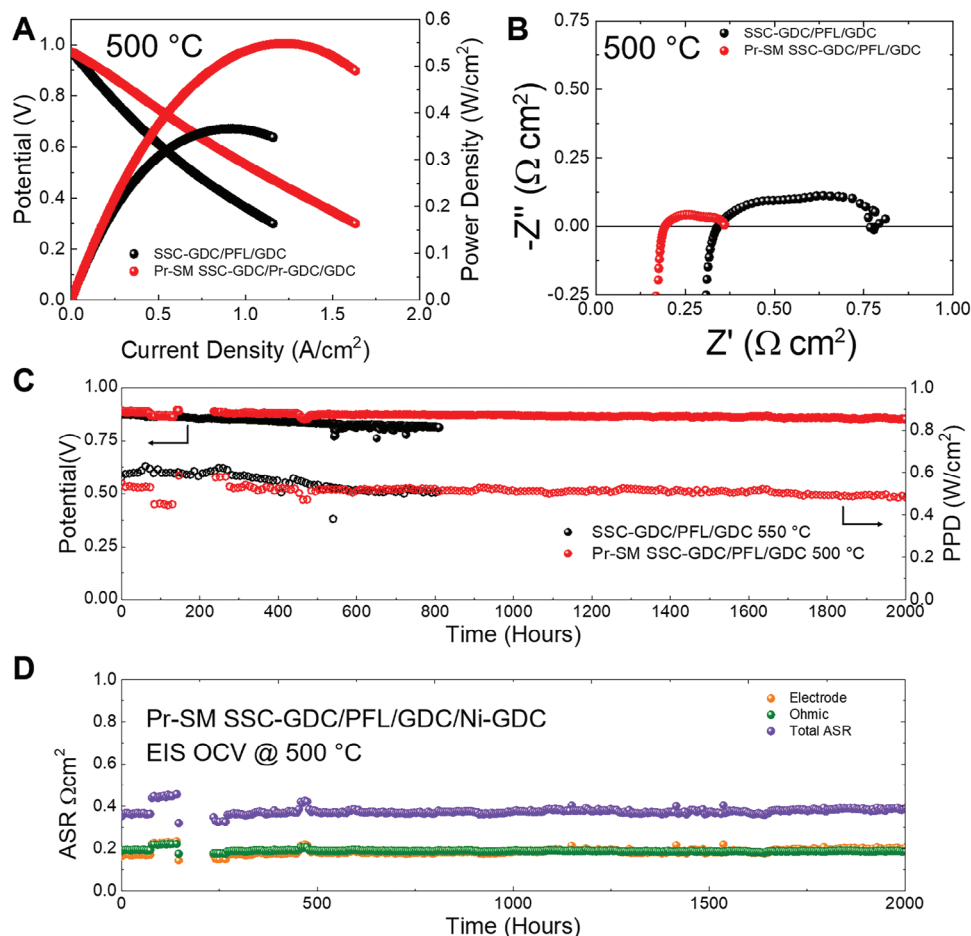


Figure 6. Performance and Stability of PFL-based SOFCs. A) iV and B) EIS of Pr-SM SSC-GDC and SSC-GDC/PFL/GDC/Ni-GDC at 500 °C. (C) SSC-GDC/PFL/GDC/Ni-GDC and Pr-SM SSC-GDC galvanostatic aging result highlighting PPD versus time (right) and D) the corresponding ASR change for Pr-SM SSC-GDC/PFL configured cell. The incident at hour 100–200 was the result of a power incident.

cathode because the use of composite cathode. Due to low concentration of Pr there is a low signal in both PFL and cathode and may just be background with slightly higher signal in PFL.

We further integrated our previous surface modification work to the PFL-based cells, and the durability and performance enhancement are highlighted in Figure 6.^[26,31] As shown in Figure 6A PFL-based SSC-GDC SOFC has a PPD of 0.35 W cm^{-2} at 500 °C in H_2 . With the Pr surface modification cathode (Pr-SM SSC-GDC), a PPD of 0.55 W cm^{-2} is reached. This result shows higher performance than a benchmark study done with a similarly configured cell.^[7] The iV result can be directly correlated to the cell impedance where the Pr-SM SSC-GDC/PFL cell has a total ASR of $0.3 \Omega \text{ cm}^2$ at 500 °C whereas the SSC-GDC/PFL has a total ASR of $0.75 \Omega \text{ cm}^2$ at 500 °C, as shown in Figure 6B. The cathode surface modification significantly lowers the cell ASR.

Cells were aged at 500 and 550 °C under 0.2 A cm^{-2} with humidified H_2 fuel, and the terminal voltage and the corresponding cell ASR are shown in Figure 6C,D, respectively. The SSC-GDC/PFL cell (black dots) shows high durability at 550 °C for over 800 h and demonstrates the porous design of the PFL can withhold its functionality even after long-term aging. Moreover,

the Pr-SM cell further enhances the performance and allows the cell to possess the same power density while operating at 50 °C lower. The modified cell shows a PPD of 0.5 W cm^2 at 500 °C with excellent stability for over 2000 h of operation. The cell ASR of the Pr-SM SSC-GDC/GDC/Ni-GDC is shown in Figure 6D, resolving the ohmic and non ohmic contributions. No major degradation appears over the course of 2000 h of operation. It is worth noting that the present work was all done using cost effective and scalable ceramic processing techniques, such as tape casting and screen printing. All parameters screened in button cells are shown in the supporting information in Figures S4, S5, and S8 and Table S1 (Supporting Information) denoting the PFL parameter being studied in Figure S8 (Supporting Information).

3. Conclusion

We address the critical electronic conduction issue in ceria-based low-temperature electrolytes by engineering defect equilibria through an external structure design. The porous design of the PFL pins the oxygen chemical potential at the PFL-DEL interface to equilibrate with air, $p\text{O}_2 = 0.21 \text{ atm}$, and, therefore, limits Ce reduction. Based on this concept, we report high-performance

LT-SOFCs over 0.55 W cm^{-2} at 500°C with over 2000 h of durability and negligible performance losses using all scalable ceramic fabrication techniques. This PFL layer dramatically increases efficiency as well as cathode activity, allowing SOFCs to operate at a much lower temperature. This work demonstrates how fundamental defect engineering can significantly impact performance at the device level and shed lights on future low-temperature electrochemical cell design.

4. Experimental Section

Material Preparation and Cell Fabrication: SOFC button cells were made using tape casting. The anode support layer (ASL) was made using an optimized tape casting method using 60 wt.% NiO (Alfa-Aesar) and 40 wt.% GDC (Fuel Cell Materials), PMMA was subsequently added to the slurry to reach desired porosity using 3 wt.% PMMA. The anode functional layer (AFL) was made also by tape casting using NiO (J.T Baker) and GDC (Fuel cell Materials) 48 and 52 wt.% respectively. The 20, 15, and 10 μm thick GDC (Fuel Cell Materials) electrolyte were made by tape casting. The ASL ($\approx 500 \mu\text{m}$ thick), AFL ($\approx 15 \mu\text{m}$ thick), and electrolyte (20, 15, and 10 μm thick) were then laminated together using a roll laminator and subsequently sintered at 1450°C for 4 h to form half cells. SSC-GDC cathode ink was made SSC (Praxair surface technologies), GDC (Fuel Cell Materials), and ESL 441 ink vehicle (Electroscience). PFL layers were made by the same process as the cathode ink, Pr_6O_{11} powder (Sigma-Aldrich) GDC (Fuel Cell Materials). PFL or SSC-GDC cathode ink was then deposited onto the Ni-GDC/GDC half-cells using a screen-printing method using a 0.31 cm^2 active area cathode. The cathode and PFL were then cofired at 950°C for 2 h. Electrolyte-supported cells were used to complete the transference number measurement study, tape cast GDC supports (200–300 μm) were sintered at 1450°C for 4 h. Ni-GDC (48% NiO- 52% GDC) ink, made the same method as the cathode ink were applied to the cell and sintered at 1200°C for 2 h. SSC-GDC/PFL was applied to the opposite and sintered at 950°C for 2 h.

To make the symmetrical cells, GDC powders were pressed using a uniaxial press to make pellets $\approx 1.5 \text{ mm}$ thick. SSC-GDC composite cathode paste and PFL (depending on the configuration) were applied to each side of the symmetrical cell and sintered at 950°C for 2 h.

Cell Infiltration: Praseodymium nitrate (Sigma-Aldrich) was dissolved in deionized water to make a 1 M Praseodymium nitrate solution. The SSC-GDC composite cathode was then infiltrated using 6 μL of 1 M Praseodymium nitrate solution. The infiltrated cathode was then placed under vacuum for 10 min. After the cell was placed under vacuum it was then fired in a furnace at 450°C for 30 min to dry the nitrate precursor.

Cell Testing: Sealing the cell consisted of using a two-part sealant (Ceramabond-517, Aremco) to a $1/2$ -inch diameter alumina tube. Gold wires and silver mesh were used as the leads and current collector and the total active area of the cell is 0.31 cm^2 limited by the cathode size. There are two thermocouples to ensure accuracy of the temperature measurement. Gas flow to the cell was controlled by mass flow controllers fixing the flow rate of hydrogen and nitrogen to 50 SCCM. Nitrogen was first used to purge the system of any air for 5 min and hydrogen was subsequently applied to the cell. The transference number of the electrolytes was determined by measuring the OCV of the SOFCs between air and H_2 / 3% H_2O at elevated temperatures. For long-term aging experiments, cells were aged at 0.2 A cm^{-2} with impedance and iV behavior pulled after 5 h of galvanostatic aging in H_2 @ 3% H_2O .

Characterization: Electrochemical measurements were performed using Solartron 1470E potentiostat coupled with Solartron 1425 frequency response analyzer or Frequency response analyzer 1260. A python script adapted from the DRT Tools package (Created by the Cicucci group) was used to perform DRT analysis.^[32] Hitachi SU-70 with X-ray Energy Dispersive spectrometer was used to acquire SEM images and EDX spectra. TESCAN XEIA FIB-SEM was used to gather ToF-SIMS data from the PFL-Electrolyte support.

Supporting Information

Supporting Information is available from the Wiley Online Library or from the author.

Acknowledgements

The authors wish to acknowledge the support of the U.S. Department of Energy, NETL Contract DEFE0031662.

Conflict of Interest

Wachsman founded company Alchemity to commercialize SOFC technology, but all results here were performed under federal contract at University of Maryland prior to the formation of Alchemity, other authors declare no conflict of interest

Data Availability Statement

The data that support the findings of this study are available from the corresponding author upon reasonable request.

Keywords

cathode, durability, ORR, SOFC, surface modification

Received: July 14, 2023
Revised: September 25, 2023
Published online: December 22, 2023

- [1] B. C. H. Steele, *Nature* **1999**, *400*, 619.
- [2] E. D. Wachsman, K. T. Lee, *Science* **2011**, *334*, 935.
- [3] E. D. Wachsman, C. A. Marlowe, K. T. Lee, *Energy Environ. Sci.* **2012**, *5*, 5498.
- [4] R. M. Ormerod, *Chem. Soc. Rev.* **2003**, *32*, 17.
- [5] S. D. Ebbesen, S. H. Jensen, A. Hauch, M. B. Mogensen, *Chem. Rev.* **2014**, *114*, 10697.
- [6] D. J. L. Brett, A. Atkinson, N. P. Brandon, S. J. Skinner, *Chem. Soc. Rev.* **2008**, *37*, 1568.
- [7] Y. Chen, B. Deglee, Y. Tang, Z. Wang, B. Zhao, Y. Wei, L. Zhang, S. Yoo, K. Pei, J. H. Kim, Y. Ding, P. Hu, F. F. Tao, M. Liu, *Nat. Energy* **2018**, *3*, 1042.
- [8] J. M. Ralph, A. C. Schoeler, M. Krumpelt, *J. Mater. Sci.* **2001**, *36*, 1161.
- [9] V. Kharton, F. Marques, A. Atkinson, *Solid State Ion.* **2004**, *174*, 135.
- [10] D. Maricle, T. Swarr, S. Karavolis, *Solid State Ion.* **1992**, *52*, 173.
- [11] I. Riess, *Solid State Ion.* **1996**, *90*, 91.
- [12] I. Riess, *Solid State Ion.* **1992**, *52*, 127.
- [13] R. J. Kee, H. Zhu, A. M. Sureshini, G. S. Jackson, *Combust. Sci. Technol.* **2008**, *180*, 1207.
- [14] K. L. Duncan, E. D. Wachsman, *J. Electrochem. Soc.* **2009**, *156*, B1030.
- [15] E. D. Wachsman, P. Jayaweera, N. Jiang, D. M. Lowe, B. G. Pound, *J. Electrochem. Soc.* **1997**, *144*, 233.
- [16] X. Zhang, M. Robertson, C. Deces-Petit, W. Qu, O. Kesler, R. Maric, D. Ghosh, *J. Power Sources* **2007**, *164*, 668.
- [17] K. L. Duncan, K.-T. Lee, E. D. Wachsman, *J. Power Sources* **2011**, *196*, 2445.
- [18] K. Eguchi, T. Setoguchi, T. Inoue, H. Arai, *Solid State Ion.* **1992**, *52*, 165.

- [19] J. Zhang, C. Lenser, N. H. Menzler, O. Guillon, *Solid State Ion.* **2020**, 344, 115138.
- [20] S. R. Bishop, T. S. Stefanik, H. L. Tuller, *J. Mater. Res. Warrendale* **2012**, 27, 2009.
- [21] Y. Chen, Y. Choi, S. Yoo, Y. Ding, R. Yan, K. Pei, C. Qu, L. Zhang, I. Chang, B. Zhao, Y. Zhang, H. Chen, Y. Chen, C. Yang, B. Deglee, R. Murphy, J. Liu, M. Liu, *Joule* **2018**, 2, 938.
- [22] Y. Chen, S. Yoo, Y. Choi, J. H. Kim, Y. Ding, K. Pei, R. Murphy, Y. Zhang, B. Zhao, W. Zhang, H. Chen, Y. Chen, W. Yuan, C. Yang, M. Liu, *Energy Environ. Sci.* **2018**, 11, 2458.
- [23] A. Leonide, SOFC modelling and parameter identification by means of impedance spectroscopy, <https://publikationen.ibliothek.kit.edu/1000019173> (accessed September 2020).
- [24] J. Hong, A. Bhardwaj, H. Bae, I.-H. Kim, S.-J. Song, *J. Electrochem. Soc.* **2020**, 167, 114504.
- [25] Y. Chen, S. Yoo, K. Pei, D. Chen, L. Zhang, B. Deglee, R. Murphy, B. Zhao, Y. Zhang, Y. Chen, M. Liu, *Adv. Funct. Mater.* **2018**, 28, 1704907.
- [26] Y.-L. Huang, A. M. Hussain, I. A. Robinson, E. D. Wachsman, *ACS Appl. Mater. Interfaces* **2018**, 10, 28635.
- [27] K.-J. Pan, A. M. Hussain, Y.-L. Huang, Y. Gong, G. Cohn, D. Ding, E. D. Wachsman, *ACS Appl. Energy Mater.* **2019**, 2, 4069.
- [28] Y.-L. Huang, C. Pellegrinelli, E. D. Wachsman, *Angew. Chem., Int. Ed.* **2016**, 55, 15268.
- [29] E. P. Murray, T. Tsai, S. A. Barnett, *Solid State Ion.* **1998**, 110, 235.
- [30] J. Fleig, H.-R. Kim, J. Jamnik, J. Maier, *Fuel Cells* **2008**, 8, 330.
- [31] Y.-L. Huang, A. M. Hussain, E. D. Wachsman, *Nano Energy* **2018**, 49, 186.
- [32] T. H. Wan, M. Saccoccio, C. Chen, F. Ciucci, *Electrochim. Acta* **2015**, 184, 483.